Inorganic Chemistry

Article

pubs.acs.org/IC

Improved Ammonolytic Synthesis, Structure Determination, Electronic Structure, and Magnetic Properties of the Solid Solution $Sn_xFe_{4-x}N$ ($0 \leq x \leq 0.9$)

Tanja Scholz and Richard Dronskowski*

Institute of Inorganic Chemistry, RWTH Aachen University, Landoltweg 1, 52056 Aachen, Germany

ABSTRACT: We report a synthetic and theoretical study of the solid solution $Sn_xFe_{4-x}N$ ($0 \leq x \leq 0.9$). A previously published ammonolytic synthesis was successfully modified to achieve the metastable nitrides in phase-pure quality out of many competing phases. As TG-DSC measurements show, the thermal stability of the nitrides increases with increasing tin content. The $Sn_xFe_{4-x}N$ series of compounds adopts an antiperovskite-like structure in space group $Pm\bar{3}m$. Various experimental and theoretical methods provide evidence that the iron substitution by tin exclusively takes place at Wyckoff position 1*a* and leads to a Vegard-type behavior of the lattice parameter over the compositional range, with an expection for a small internal miscibility gap around $Sn_{0.33}Fe_{3.67}N$ of unknown cause. For highly tin-substituted iron nitrides the composition was clarified by prompt gamma-ray activation analysis (PGAA) and determined as $Sn_{0.78(3)}Fe_{3.22(4)}N_{0.95(3)}$ evidencing a fully occupied nitrogen position. Magnetic measurements reveal a linear weakening of ferromagnetic interactions with increasing tin concentration.

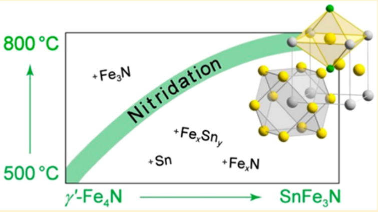

INTRODUCTION

The binary and ternary nitrides of iron exhibit exciting chemical and physical properties, as exemplified by the archetype γ'-Fe_4N with its exceptional mechanical hardness and magnetic properties, e.g., a large saturation magnetization of 208 emu g^{-1} and a low coercivity of $H_C = 5.8$ Oe ≈ 460 A m^{-1}.[1,2] In combination with γ'-Fe_4N's large corrosion resistance, these properties make the phase a candidate for magnetic recording applications.[3−5] γ'-Fe_4N adopts a simple antiperovskite-like structure in space group $Pm\bar{3}m$ with a lattice parameter of 3.8009(1) Å.[6] Iron atoms occupy the cube's corners (Wyckoff position 1*a*) and faces (3*c*) while nitrogen is located in the 1*b* octahedral centers (Figure 1). Furthermore, it is known that substituting iron atoms on Wyckoff positions 1*a* and/or 3*c* may tune the magnetic and mechanical properties in terms of desired applications. Therefore, many nitrides with the general formula $M_xFe_{4-x}N$ have been studied in order to arrive at new materials for better technologies.

The first investigation of the iron−tin−nitrogen system and, in particular, $Sn_xFe_{4-x}N$ was published by Stadelmeier and Fraker in 1962.[7] The ternary nitride phase was synthesized from precursor alloys containing 10%, 20%, and 25% tin within an iron matrix using a classical NH_3/H_2 ammonolytic reaction at 600 °C. Although no diffraction patterns were given, the phase was reported to adopt the aforementioned antiperovskite structure. The alloy with the highest tin:iron ratio of 1:3 corresponds to the daltonide $SnFe_3N$ with a lattice parameter of $a = 3.90$ Å. When iron is substituted by tin, the unit cell expands in a Vegard-like behavior that is known for numerous ternary iron nitrides $M_xFe_{4-x}N$. In general, the substitution takes place at either one of the iron positions or on both sites (1*a* and/or 3*c*) simultaneously, and it depends on the covalent or metallic radius and, furthermore, on the metal's affinity to the central nitrogen atom on 1*b*. As a general rule discussed in detail in ref 6, large metal atoms prefer the larger cuboctahedral 1*a* environment (an approximate sphere with $r = 1.42$ Å) as compared to the smaller 3*c* position (1.28 Å). In another study concerning $Sn_xFe_{4-x}N$, Li et al.[8] claimed that, despite the large radius of tin ($r_M(Sn) = 1.62$ Å,[9] $r_{cov}(Sn) = 1.39$ Å[10]), the substitution would take place on *both* 1*a* and 3*c* positions and result in a maximum tin content of $Sn_{1.2}Fe_{2.8}N$ with $a = 3.843$

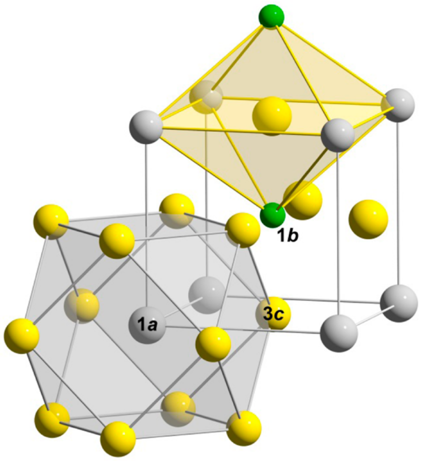

Figure 1. Crystal structure of γ'-Fe_4N and $M_xFe_{4-x}N$ in space group $Pm\bar{3}m$. The green nitrogen atom occupies the very center (Wyckoff position 1*b*) while the cube's corners (1*a*) and face centers (3*c*) are occupied by iron in γ'-Fe_4N. Substituting the iron atoms by other metal atoms occurs on the Wyckoff positions 1*a* and/or 3*c*.

Received: July 6, 2015
Published: August 19, 2015

DOI: 10.1021/acs.inorgchem.5b01510
Inorg. Chem. 2015, 54, 8800−8807

Å. This corresponds to a tiny (3.3%) unit-cell expansion of γ'-Fe_4N due to Sn incorporation which we will address in our results. Furthermore, Li et. al provided Mößbauer data for $Sn_xFe_{4-x}N$[8,11] and compared their findings to preliminary Mößbauer results by Andriamandroso et al., who found a preferential substitution on the 1*a* lattice site.[12] We also note that there have been theoretical studies targeted at the properties of $SnFe_3N$ assuming a ferromagnetic ground state,[13−15] but up to now, no comprehensive experimental *and* theoretical investigation of $Sn_xFe_{4-x}N$ has been communicated.

In their early study[7] Stadelmeier and Fraker applied the classical NH_3/H_2 ammonolytic reaction as the common synthetic route to achieve binary and ternary nitrides. Recently, this very approach has been improved by a two-step ammonolytic method combining a high-temperature sintering reaction (1000−1250 °C) and a low-temperature nitriding step (300−700 °C)[16] to yield, for example, $Rh_xFe_{4-x}N$,[16] $Ga_xFe_{4-x}N$,[17] $In_xFe_{4-x}N$,[18] and $PdFe_3N$[19] with phase-pure quality. In both types of ammonolyses the nitride is formed during the nitriding step while the intermediate temperature ramps have to be carefully chosen to yield the favored nitride competing with other compounds of similar energy in the phase systems. Also, the syntheses can be run either under thermodynamically or kinetically controlled conditions to achieve the desired nitride.

In the present study, we investigate the entire $Sn_xFe_{4-x}N$ series of compounds from a synthetic point of view, and the results are compared to extensive density-functional (DFT) calculations. In fact, the thermodynamic stability of $Sn_xFe_{4-x}N$ has been evaluated first for optimizing the two-step ammonolytic synthesis. Also, the structural properties are derived from powder X-ray diffraction to shed new light on the Vegard-like behavior and the actual iron substitution by tin on 1*a* and/or 3*c*. Finally, the magnetic properties of the entire series of compounds are determined and compared with theoretical data.

■ EXPERIMENTAL AND COMPUTATIONAL METHODS

Synthesis of $Sn_xFe_{4-x}N$. The powdered reactants Sn and Fe_2O_3 were mixed and accurately ground using the desired metal-atom ratio. A two-step ammonolytic reaction gave access to phase-pure $Sn_xFe_{4-x}N$. The ammonolysis gas was a mixture of NH_3 (5.6 mL min^{-1}) and H_2 (8.4 mL min^{-1}). For a detailed description of the reaction conditions, see Results and Discussion.

XRPD and Rietveld Refinement. X-ray diffraction of $Sn_xFe_{4-x}N$ at room temperature was performed using a calibrated STADI MP (STOE Darmstadt) powder diffractometer with Mo $K\alpha_1$ radiation (λ = 0.709 320 Å, flat sample, 8° $\leq 2\theta \leq$ 130°, step rate 0.01° in 2θ). Rietveld refinements were carried out with the program FullProf[20] using a pseudo-Voigt profile function for which the axial divergence asymmetry was accounted for up to 30° in 2θ. The patterns were refined in space group $Pm\bar{3}m$ (No. 221) with the Wyckoff positions 1*a* for tin, 1*b* for nitrogen, and 1*a*/3*c* for iron. The mixed occupations of tin and iron atoms on 1*a* were constrained to unity, as were the full occupations of iron on 3*c* and of nitrogen on 1*b*. The refinement parameters and the residual values are listed in Table 3.

TG-DSC. Thermal decomposition and phase transitions were recorded with simultaneous thermogravimetry−differential scanning calorimetry using a Netzsch STA 449 C calorimeter. The experiments were conducted in argon flow (25 mL min^{-1}) from room temperature to 1200 °C with a heating rate of 20 K min^{-1}.

PGAA. A prompt gamma-ray activation analysis[21] was performed at the Forschungs-Neutronenquelle Heinz Maier-Leibnitz (FRM II) in Garching. A white cold neutron beam with an intensity of 2×10^9 n cm^{-2} s^{-1} of thermal equivalent and average wavelength of 6.8 Å was used. Data acquisition was done by a standard Compton-suppressed gamma spectrometer consisting of one HPGe detector with relative efficiency of 60% (ORTEC PopTop n-type) inserted in an annulus BGO scintillator (coaxial geometry). The sample was sealed to a standard PTFE bag and held on a Teflon ladder to minimize the counting background. Also, the sample chamber was evacuated in order to suppress the gamma-ray background coming from the neutron capture on air which is especially important for the detection of nitrogen within the sample. The acquisition time of the $Sn_{0.8}Fe_{3.2}N$ sample was 12 h, where the background signal from the PTFE bag was later subtracted by a standard procedure.

SQUID Magnetometry. The magnetic properties of all samples were determined by SQUID magnetometry (MPMS-5S, Quantum Design). Temperature-dependent measurements in the temperature range 2−400 K were carried out at applied fields of B_0 = 0.01 and 0.1 T. Hysteretic loops were recorded at a temperature of 5 K within a field range of $B_0 = \pm 5$ T.

Computational Details. Theoretical calculations of the structural and electronic properties were carried out using the Vienna *ab initio* simulation package (VASP)[22−24] based on density-functional theory (DFT) using projector-augmented-wave (PAW) potentials[25,26] for core and valence electron separation. Exchange and correlation contributions were treated with the generalized gradient approximation as parametrized by Perdew, Burke, and Ernzerhof (GGA-PBE).[27] An 8 × 8 × 8 Monkhorst−Pack[28] *k*-point grid for one supercell containing eight formula units was used for Brillouin-zone integration while the energy-cutoff was set to 500 eV. Spin-polarized calculations for ferromagnetic and antiferromagnetic cases were performed with integer starting values for all local magnetic moments, namely, 3 for all magnetically active elements and 0 for all other elements. Forces, stress tensors, atomic positions, unit cell shapes, and unit cell volumes of the crystal structures were allowed to relax during optimization. Because of the expected small energy differences, the convergence criterion of the electronic-structure calculation was set to 0.01 meV.

■ RESULTS AND DISCUSSION

Stability. To better understand the thermochemistry of the aforementioned tin iron nitrides, the relative stability of the daltonide $SnFe_3N$ was calculated prior to synthesis. Hence, density-functional theory (DFT) was applied to quantify the enthalpies of $SnFe_3N$ at absolute zero temperature as compared to the most likely competing phases. Although iron(III) oxide is experimentally used as a reactant, it is important to understand that elemental iron is the correct reference phase because it is instantly formed through oxide reduction in the hydrogen flow. Furthermore, a ferromagnetic ordering is assumed in the quantum-mechanical calculations. Although antiferromagnetic ordering is discussed in the later paragraphs, the energetic differences introduced by different magnetic states are relatively small.

Table 1 shows two possible reaction schemes giving $SnFe_3N$. The first reaction can be understood as the incorporation of tin into ε-Fe_3N resulting in a ternary compound; alternatively, because the reaction is endothermic, it may be looked upon as the decomposition of the ternary compound into ε-Fe_3N and

Table 1. Theoretical Relative Stability of $SnFe_3N$ at Absolute Zero Temperature (0 K) in Comparison to the Most Likely Competing Phases

reaction	ΔH_R/kJ mol^{-1}
(1) Sn + ε-Fe_3N → $SnFe_3N$	+14.3
(2) Sn + γ'-Fe_4N → $SnFe_3N$ + α-Fe	+5.7

elemental tin. It is already known from the binary iron—nitrogen system that γ'-Fe_4N, with a narrow homogeneity range regarding the nitrogen content, decomposes to ε-Fe_3N_{1+x} with a wide homogeneity range at elevated temperature (680 °C).[29] With this in mind, we need to pay special attention to ε-Fe_3N_{1+x} as a competing side phase. Additionally, the substitution of iron in γ'-Fe_4N by tin characterizes the second reaction which is also endothermic. That is to say that, at absolute zero temperature, the binary nitride is preferred over the ternary nitride such that the reaction has to be carefully controlled in terms of reaction temperatures as well as heating and cooling rates to eventually yield the *metastable* tin iron nitride.

Synthesis. The entire series of tin iron nitrides $Sn_xFe_{4-x}N$ was synthesized as single-phase powders except for a very small and confined compositional range where an apparent two-phase region was detected (addressed later on). The nitrides were prepared via a route similar to the aforementioned two-step ammonolytic reaction (Figure 2) but carefully modified in terms of individual temperatures and time profiles. In contrast to the synthesis of $Rh_xFe_{4-x}N$,[16] $Ga_xFe_{4-x}N$,[17] $In_xFe_{4-x}N$,[18] and $PdFe_3N$[19] where the reactants were inserted in the furnace at elevated temperatures (1000−1200 °C), the ground reactants iron(III) oxide and elemental tin were slowly heated, especially near the melting point of tin (210−250 °C), before the actual sintering reaction took place at 1100 °C. Generally, ternary nitrides $M_xFe_{4-x}N$ are formed in the subsequent nitriding step, and it is usually sufficient to choose one nitridation temperature in the range 300−700 °C for the entire series of compounds. For metastable $Sn_xFe_{4-x}N$, however, this did not result in phase-pure products. In the end, the chosen temperature had to fit into a rather narrow and carefully controlled nitridation corridor to avoid side-phases (Figure 3). The latter were known as competing phases from previous DFT investigations. In detail, we observed ε-Fe_3N_{1+x} impurities due to the decomposition of $Sn_xFe_{4-x}N$ if the nitriding temperature was too high. If it was too low, the product appeared as inhomogeneous with large amounts of intermetallic Fe−Sn compounds, binary iron nitrides, and even elemental tin. Additionally, the composition of the ammonolysis gas had to be changed from the common 1:1 ratio for the NH_3:H_2 mixture to 2:3; thereby, the nitriding potential or, in other words, the activity of atomic nitrogen was lowered upon reaction. In order to obtain crystalline and phase-pure powders of $Sn_xFe_{4-x}N$, the nitriding reaction had to be repeated after grinding the intermediate inhomogeneous and poorly crystalline products.

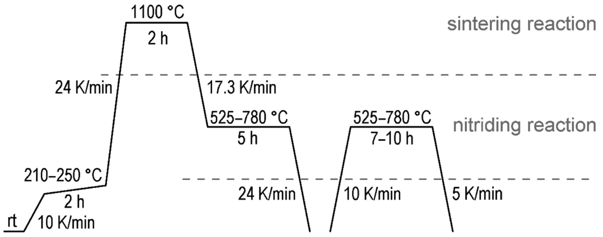

Figure 2. Schematic diagram of the ammonolytic reaction with a sintering step (1100 °C) and a nitriding step (525−780 °C) as main reactions. To improve the quality of the product, the nitriding reaction has to be carried out twice.

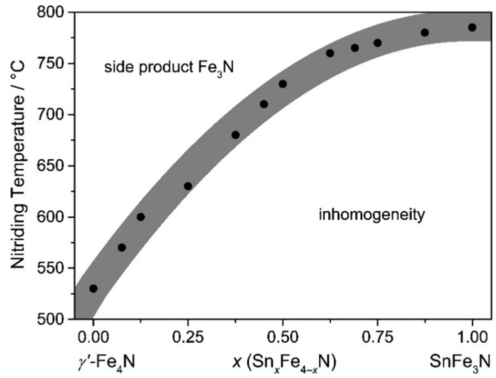

Figure 3. Temperature corridor for the nitriding reaction as a function of the intended composition of $Sn_xFe_{4-x}N$.

Since tin iron nitrides $Sn_xFe_{4-x}N$ are only accessible in a rather narrow nitridation-temperature corridor, we determined the stability of the nitrides by thermal analysis (TG-DSC) with an argon carrier gas. The mass loss in the DTG was assigned to nitrogen and started at 680 °C for the roughly half-substituted $Sn_{0.55}Fe_{3.45}N$ and, at 730 °C, for the highly diluted $Sn_{0.88}Fe_{3.12}N$. The DSC showed two exothermic signals at 930 and 1120 °C that refer to peritectic decompositions of iron tin alloys. An XRPD pattern of the TG-DSC residue reveals only iron tin alloys. We conclude from that experiment that the decomposition temperatures of the nitrides are below the optimized nitridation temperatures in an ammonia/hydrogen atmosphere, highlighting the nitrides' *metastable* nature. In any case, the decomposition temperatures increase with the tin amount, corroborating the increase in the nitrides' thermal stability.

Structure and Composition. The structural characterization was carried out using powder X-ray diffraction and Mo Kα_1 radiation (λ = 0.709 320 Å). Its major advantages as compared to commonly used Cu Kα_1 radiation (λ = 1.540 59 Å) are given by the suppression of a significant fluorescence background (mirroring the high iron content of $Sn_xFe_{4-x}N$) and, because of that, an improved intensity-to-background ratio as well as better overall statistics due to more accessible reciprocal space in the same 2θ angular range ($8° \leq 2\theta \leq 130°$). For the gallium-substituted $Ga_xFe_{4-x}N$ series of compounds, their lattice parameters and mixed occupations have already been accurately determined using Mo Kα_1 radiation.[6] The superb quality of the X-ray powder pattern and the Rietveld refinement for the highly diluted $Sn_{0.88}Fe_{3.12}N$ are exemplarily shown in Figure 4.

Returning to the early question whether or not tin atoms occupy the Wyckoff positions 1*a* and/or 3*c*, the excellent X-ray diffraction patterns reveal (almost, see below) single-phase powders just up to an intended tin content x = 0.875 ($Sn_{0.875}Fe_{3.125}N$). This leads us to believe that tin atoms exclusively occupy the Wyckoff position 1*a*. Also, the Rietveld refinements are only successful if a mixed tin/iron occupation at the corner position (1*a*) is performed while constraining the sum of the occupation parameter to unity. Thus, the faces of the unit cell (3*c*) are exclusively occupied by iron atoms.

To further support the above claim about the preferred substitution, the distribution of tin over both Wyckoff positions was theoretically analyzed for $SnFe_3N$. Tin atoms can either occupy 1*a* or 3*c* resulting in ordered phases $^{1a}(Sn)^{3c}(Fe_3)^{1b}(N)$ and $^{1a}(Fe)^{3c}(SnFe_2)^{1b}(N)$, respectively. Furthermore, tin atoms can be statistically disordered as in $^{1a}(Sn_{1/4}Fe_{3/4})^{3c}(Sn_{3/4}Fe_{9/4})^{1b}(N)$. From the energetic results

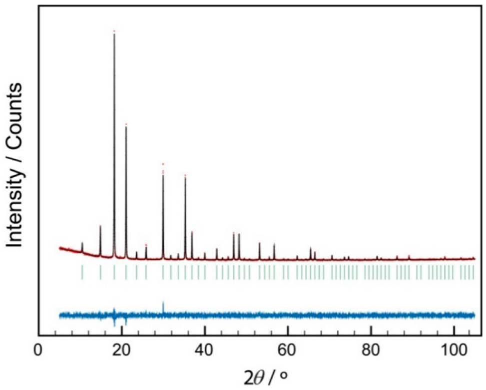

Figure 4. X-ray diffraction pattern plot and Rietveld refinement of $^{1a}(Sn_{0.88})^{1a}(Fe_{0.12})^{3c}(Fe_3)^{1b}(N)$ ($Pm\bar{3}m$, a = 3.8818(1) Å) measured with Mo Kα1 radiation. The vertical bars designate the positions of the Bragg reflections.

listed in Table 2 it is obvious that the tin atoms exclusively occupy the larger corner position 1*a* because that scenario is energetically favored by an enormous 85 kJ mol^{-1} over a statistically disordered arrangement. Also, the calculated lattice parameter (3.89 Å) of $^{1a}(Sn)^{3c}(Fe_3)^{1b}(N)$ is in excellent agreement with the experimental result ($^{1a}(Sn_{0.88})^{1a}(Fe_{0.12})^{3c}(Fe_3)^{1b}(N)$, a = 3.8818(1) Å), whereas the two other theoretical models both arrive at values that are far too large, beyond 4 Å. To conclude, syntheses, structure analyses, and theoretical investigations confirm the $^{1a}(Sn_xFe_{1-x})^{3c}(Fe_3)^{1b}(N)$ type of ordering.

Table 2. Total Energy Differences ΔE per Unit Cell between Different Atomic Arrangements on Wyckoff Positions 1*a* and 3*c*[a]

	ΔE/kJ mol^{-1}	a/Å
$^{1a}(Sn)^{3c}(Fe_3)^{1b}(N)$	0	3.89
$^{1a}(Sn_{1/4}Fe_{3/4})^{3c}(Sn_{3/4}Fe_{9/4})^{1b}(N)$	+85	4.06
$^{1a}(Fe)^{3c}(SnFe_2)^{1b}(N)$	+126	4.10

[a] Relative to the ordered occupation $^{1a}(Sn)^{3c}(Fe_3)^{1b}(N)$ and the corresponding lattice parameters a in the antiperovskite-like structure type. The calculated data are based on spin-polarized (ferromagnetic) VASP PAW GGA-PBE calculations.

After having located the substitutional site, we will now concentrate on the substitutional effect for the entire $Sn_xFe_{4-x}N$ series of compounds with $x \leq 1$. The results of the Rietveld refinements are summarized in Table 3 and displayed in Figure 5.

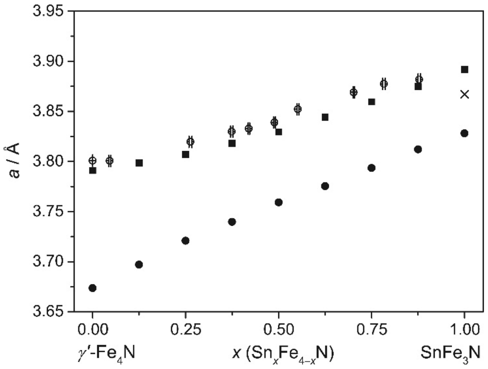

Figure 5. Change of experimental lattice parameter a based on the refined composition for the $Sn_xFe_{4-x}N$ series of compounds (○). The error bars indicate the uncertainty of the occupation on position 1*a*. Theoretical lattice parameters are based on a ferromagnetic (■), antiferromagnetic (×), and a nonmagnetic model (●).

As shown in the evolution of the experimental lattice parameter a (Figure 5), substituting iron by tin atoms on 1*a* leads to a continuous increase of a in a Vegard-type behavior. The nitride richest in tin, namely, $Sn_{0.878(3)}Fe_{3.122(3)}N$, has a lattice parameter of a = 3.8818(1) Å, equivalent to a unit-cell expansion of 6.5%. Back in 1962, Stadelmeier and Fraker arrived at a value of a = 3.90 Å.[7] These moderate increases are about twice as large as the one reported by Li et al.[8] and look reasonable, keeping the large metallic/covalent radii of tin in mind. Li et al., however, arrived at a = 3.843 Å such that, utilizing our results as stoichiometric standards, Li's compound corresponds to a tentative composition of $Sn_{0.5}Fe_{3.5}N$ instead of the claimed $Sn_{1.2}Fe_{2.8}N$ with tin on positions 1*a* and 3*c*.

In addition, theoretical lattice parameters were computed assuming different magnetic ground states. There were 2 × 2 × 2 supercells with apparently random-like distributions of iron and tin atoms on 1*a* generated preserving the cubic metric, and different metal atom ratios were realized. Among these supercells, the ones with identical compositions but being lowest in energy were included in the final analysis (see Figure 5). The calculated pseudocubic lattice parameters (by volume averaging) for a ferromagnetic (FM) model are in excellent agreement with the experimental ones, with a maximum deviation of less than 1%. The nonmagnetic model does not explain the Vegard-type behavior satisfactorily and was

Table 3. Intended Composition x of the $Sn_xFe_{4-x}N$ Series, Refined Lattice Parameter a, Refined Sn Occupation on the 1*a* Position $^{1a}x_{occ}(Sn)$, Related Profile and Bragg Residual Values R_P and R_B, Molar Mass M, and X-ray Density ρ

x	a/Å	$^{1a}x_{occ}$(Sn)	R_P/%	R_B/%	M/g mol^{-1}	ρ/g cm^{-3}
0[6]	3.8009(1)				237.39	7.18
0.04	3.8007(1)	0.046(3)	2.98	4.49	240.28	7.27
0.25	3.8208(1)	0.276(3)	3.32	3.55	253.92	7.58
0.35	3.8299(1)	0.374(3)	3.17	4.03	260.90	7.71
0.375	3.8328(1)	0.420(2)	3.13	3.42	263.79	7.74
0.45	3.8390(1)	0.489(2)	3.17	2.13	268.13	7.87
0.5	3.8521(1)	0.552(2)	3.09	2.36	272.09	7.90
0.69	3.8691(1)	0.702(2)	3.55	2.68	281.52	8.07
0.75	3.8774(1)	0.783(3)	3.69	3.34	286.61	8.17
0.875	3.8818(1)	0.878(3)	4.03	3.68	292.58	8.29

DOI: 10.1021/acs.inorgchem.5b01510
Inorg. Chem. 2015, 54, 8800−8807

excluded from further studies. Additionally, an antiferromagnetic (AFM) ground state was considered for the complete $SnFe_3N$ constitution. While the details about different AFM spin arrangements will be discussed later, the lattice parameter for the most favorable AFM cell type is only 1% smaller than in the FM case. Because a complete substitution of iron by tin on 1*a* has not been experimentally accomplished, we cannot say with certainty whether the highly tin-diluted iron nitride exhibits FM or an AFM order solely on the basis of the lattice parameter.

The lattice parameter, however, not only depends on the metal ratio but is also strongly influenced by the nitrogen concentration neglected so far. This is common practice in nitride research because site-occupation refinements of light elements are hardly reliable from powder XRD data; the problem is less important for the archetype γ'-Fe_4N with only a small phase width regarding the nitrogen content.[29] Still, it is well-known that the iron nitride of the lighter homologous element Ge has a limited nitrogen capacity ($y \ll 1$) for large substitutional degrees.[30] Thus, prompt gamma-ray activation analysis (PGAA) measurements[21] were performed at FRM II, Garching, to determine the bulk elemental composition of a highly tin-substituted iron nitride whose composition had been characterized as $Sn_{0.783(3)}Fe_{3.217(3)}N_y$ by powder XRD Rietveld refinements. The sample was measured with a standard PGAA setup without an internal standard such that the analysis gave only *relative* compositions. We further assumed full occupation of the metal positions 1*a* and 3*c* and an exclusive tin occupation on 1*a* which translates into a site-occupation equation ${}^{1a}x^{Sn} + {}^{1a}x^{Fe} + {}^{3c}x^{Fe} = 4$. The renormalized PGAA results yield the composition $Sn_{0.78(3)}Fe_{3.22(4)}N_{0.95(3)}$, in excellent agreement with the XRD-derived composition of the crystalline phase. Furthermore, it is obvious that the nitrogen content of the highly tin-substituted compound is unity within experimental resolution, and we conclude that there is no limited nitrogen capacity in the entire $Sn_xFe_{4-x}N_y$ series of compounds.

For the solid solution $Sn_xFe_{4-x}N$ the structural data imply an almost perfect substitution of iron by tin with a Vegard-type behavior. Nonetheless, a very close look into the composition range between $Sn_{0.25}Fe_{3.75}N$ (refined: $Sn_{0.28}Fe_{3.74}N$) and $Sn_{0.35}Fe_{3.65}N$ (refined: $Sn_{0.37}Fe_{3.63}N$) reveals asymmetric or even split reflections in the X-ray diffraction pattern (Figure 6) which cannot be cured by further synthetic optimization, e.g., modified reaction temperatures and temperature ramps, duration of the sintering and nitriding steps, and ammonia and hydrogen gas flows. Even when introducing a second nitridation step after grinding, the phenomenon persists. It seems as if iron and tin atoms would not mix between the two aforementioned phases, boundary phases that should *not* exist according to Vegard's law. In-between compositions result in two-phase products with portions according to the intended atom ratio. For an intended composition $Sn_{0.33}Fe_{3.67}N$ the intensity of the split reflections are about the same such as to imply the very center of an internal and entirely unexpected and somewhat mysterious miscibility gap. Until now, we cannot explain this anomaly that has never been observed before in ternary $M_xFe_{4-x}N$ nitrides. The phenomenon deserves further study, apparently with a more local probe.

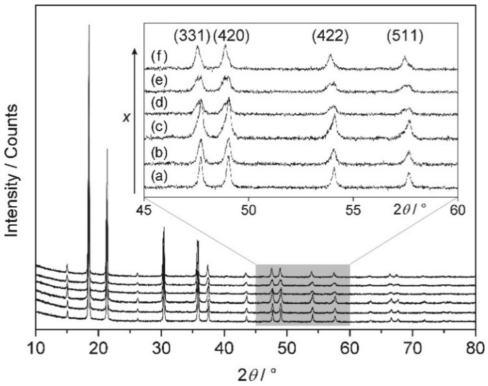

Figure 6. X-ray diffraction pattern of $Sn_xFe_{4-x}N$ with the intended compositions x = (a) 0.25, (b) 0.27, (c) 0.29, (d) 0.31, (e) 0.33, and (f) 0.35. Only parts a and f show phase-pure quality and result in the Rietveld refined compositions with x = (a) 0.276(3) and (f) 0.374(3).

Magnetic Characterization. To tune the magnetic properties with regard to desired applications, iron atoms in γ'-Fe_4N can be substituted by other atoms. Therefore, tin substitution into γ'-Fe_4N has also been magnetically studied. The magnetic properties of the entire $Sn_xFe_{4-x}N$ series were determined by SQUID magnetometry (MPMS-5S, Quantum Design). The susceptibility was measured in the temperature range 2−400 K (Figure 7). The course of the molar susceptibility suggests that low degrees of tin substitutions lead to ferromagnetic compounds with Curie temperatures above room temperature while high degrees result in small molar susceptibilities with pronounced maxima at low temperatures (ca. 13 K for $Sn_{0.878(3)}Fe_{3.122(3)}N$). Atomic substitution affects the magnetic properties continuously so that intermediate substitutional degrees show broad susceptibility maxima.

To further investigate the magnetic properties of $Sn_xFe_{4-x}N$, hysteretic loops were recorded at a temperature of 5 K within a field range of $B_0 = \pm 5$ T (Figure 8, top). Clearly, the magnetic moments decrease with increasing tin concentration. Also, only the hysteretic loops of lower tin-substituted nitrides ($x = 0.046$ and 0.263) appear as being saturated whereas the phases with higher tin substitutions only approach the magnetic saturation at $B_0 = \pm 5$ T. Nonetheless, the experimental atomic saturation magnetization as well as the experimental unsaturated magnetic moments at $B_0 = \pm 5$ T show a perfect linearity decreasing from 8.96 μ_B for γ'-Fe_4N[17] to 1.02 μ_B for the tin-richest $Sn_{0.878(3)}Fe_{3.122(3)}N$ (Figure 8, bottom). That is to say that substituting iron by tin weakens the ferromagnetic coupling. If the experimental data are extrapolated to a daltonide $SnFe_3N$, they even suggest a zero magnetic moment. Upon comparing the experimental trend with theoretical saturation moments, a FM model fits best to γ'-Fe_4N, with the slight overestimation going back to the chosen GGA parametrization,[27] while the AFM model fits $SnFe_3N$ which, however, could not be experimentally prepared. In any case, we did not find any magnetic anomaly that would explain the internal miscibility gap around $Sn_{0.33}Fe_{3.67}N$ as described above.

Reiterating the course of the experimental saturated and unsaturated atomic moments, an AFM ordering for daltonide $SnFe_3N$ seems reasonable. To gain more insight into those spin arrangements, a thorough theoretical study was conducted on the basis of a concept that had already been used successfully for AFM ordering of iron spins in a supercell of $GaFe_3N$.[6] This concept had originally been derived from a neutron diffraction study on perovskite-like structures of the type $(La_{1-x}Ca_x)MnO_3$ for which a total number of seven AFM spin arrangements was modeled.[31] We refer the reader to ref 6 for a detailed discussion of the AFM models. Figure 9 shows the energy difference

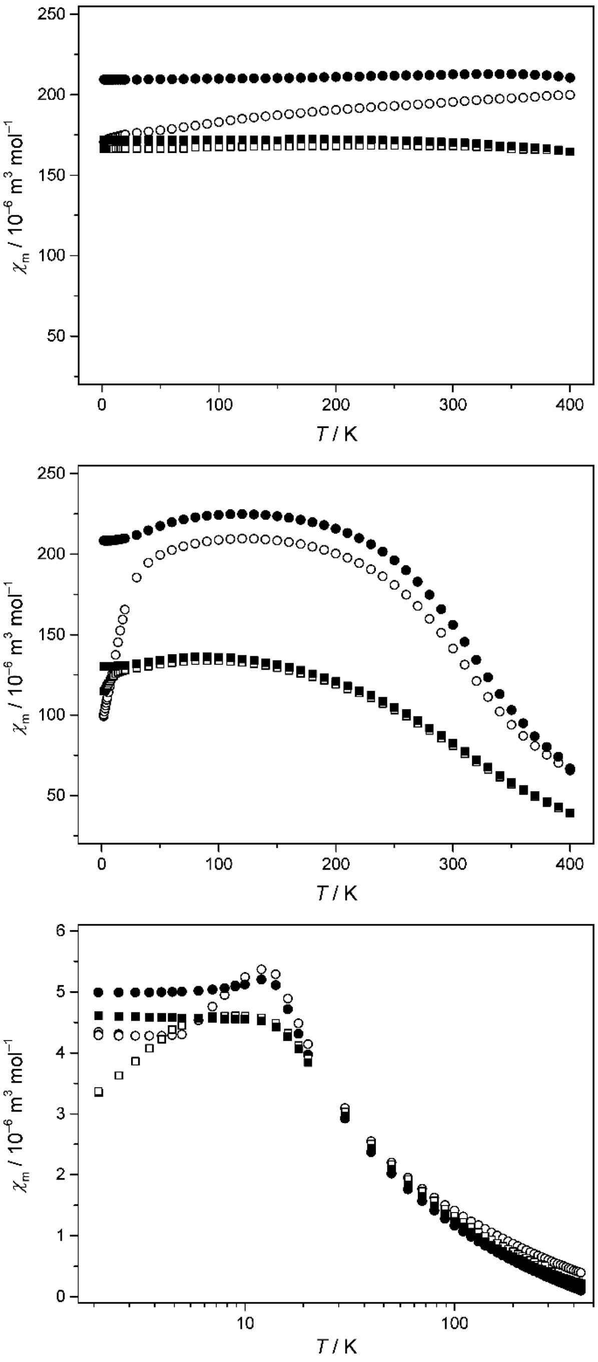

Figure 7. Molar susceptibility of $Sn_xFe_{4-x}N$ with the Rietveld refined compositions $x = 0.276(3)$ (top), $0.552(2)$ (middle), and $0.878(3)$ (bottom) as a function of temperature, T. Different measurement conditions were applied: (●) field-cooled, $B_0 = 0.01$ T; (○) zero-field-cooled, $B_0 = 0.01$ T; (■) field-cooled, $B_0 = 0.1$ T; (□) zero-field-cooled, $B_0 = 0.1$ T.

between these seven AFM spin arrangements dubbed A–G while the simple FM case of $SnFe_3N$ is used as a reference. All AFM arrangements differ from each other by less than 14 kJ mol^{-1}, and they even have about the same energy as the FM structure. In fact, two of the AFM cells are even more stable than the FM model (indicated by a negative energy difference), but the amount of less than 2 kJ mol^{-1} is on the order of the DFT accuracy. Nonetheless, for high tin contents AFM interactions become increasingly important.

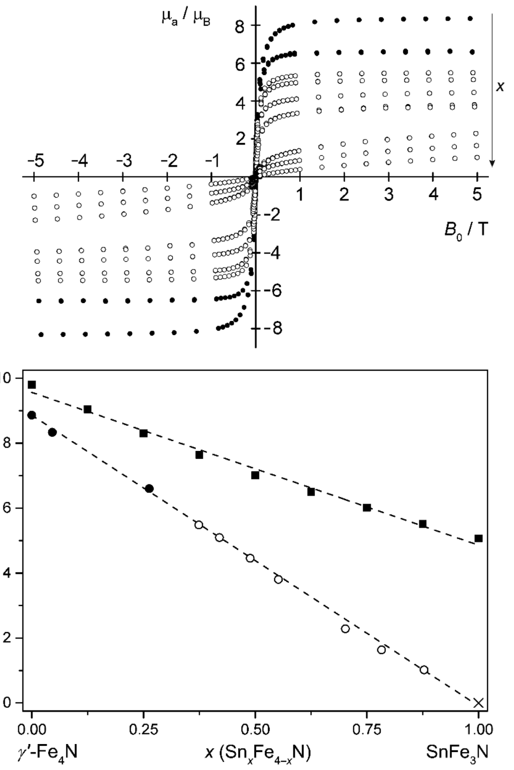

Figure 8. Top: Hysteretic loops of the $Sn_xFe_{4-x}N$ series with the Rietveld refined compositions $x = 0.046(3)$, $0.263(3)$, $0.374(3)$, $0.420(2)$, $0.489(2)$, $0.552(2)$, $0.702(2)$, $0.783(3)$, and $0.878(3)$ at a temperature of 5 K. The magnetic moments μ_a decrease with increasing tin concentration. Hysteretic loops either reach saturation within the applied field (●) or do not (○). Bottom: Change of corresponding experimental atomic saturation moments μ_a^s (●), and experimental unsaturated moments μ_a (○) in comparison to the theoretical atomic saturation moments of an FM model (■) for the $Sn_xFe_{4-x}N$ series and the AFM model (×) for $SnFe_3N$. Dashed lines are intended to guide the eyes.

A second look at the different AFM arrangements A–G shows that the energetically most favorable ones are A- and B*-type cells which exhibit a large number of FM interactions between neighboring iron atoms along all spatial directions. In contrast, the highest-energy G-type structure is predominantly characterized by AFM interactions. In line with this, structures of the "intermediate" cell types (C–F) result in intermediate energies.

Both experiment and modeling indicate the importance of AFM interactions in highly tin-substituted iron nitrides, but FM interactions cannot be neglected. Upon going from γ'-Fe_4N to $SnFe_3N$, the magnetism changes due to a weakening of the FM coupling. This concept is known from short-range RKKY-type interactions in random alloys in which neighboring impurities are strongly coupled ferro- or antiferromagnetically and form magnetic clusters because of concentration fluctuations.

■ CONCLUSIONS

An improved two-step ammonolysis reaction gives access to metastable $Sn_xFe_{4-x}N$ $(0 \leq x \leq 0.9)$. To achieve the compounds in phase-pure quality it is especially important to choose the right nitridation temperature such that it lies within a rather narrow temperature corridor. The decomposition of the compounds was analyzed by TG-DSC and starts below the optimized nitridation temperatures, thereby emphasizing the

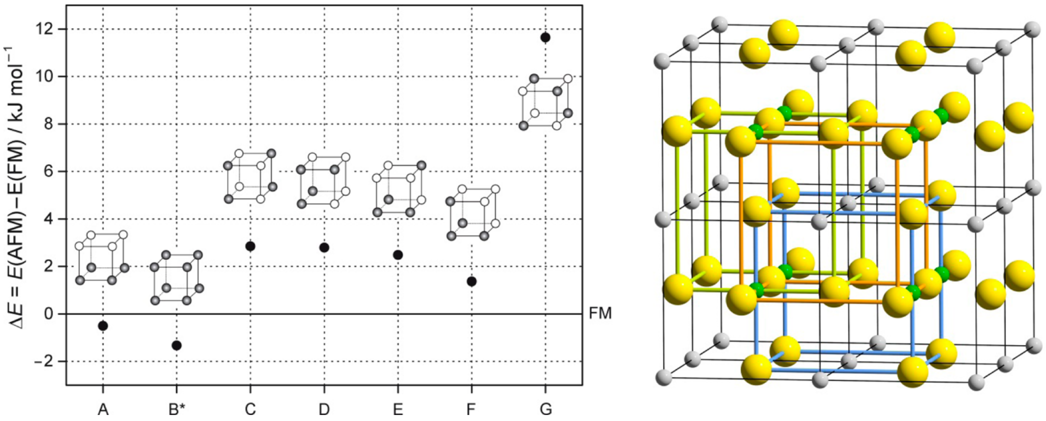

Figure 9. Left: Energy difference between different AFM spin arrangements (A−G) and the ferromagnetic ordering in $SnFe_3N$. Primitive unit cells illustrate the different spin arrangements of iron atoms in which empty and filled circles relate to opposite directions of spins. Right: Three of these primitive iron cells (colored green, orange, and blue) are arranged in the $SnFe_3N$ supercell. Note: The B*-type cell is constructed from two B-type subgrids with opposite spin-alignments and one A-type subgrid. For a detailed explanation of the concept see ref 6.

nitrides' metastable nature. The $Sn_xFe_{4-x}N$ series of compounds adopts an antiperovskite-like structure ($Pm\bar{3}m$) and shows a Vegard-type behavior of the lattice parameter except for an internal miscibility gap around $Sn_{0.33}Fe_{3.67}N$ of unknown cause. For the highly tin-substituted $Sn_{0.878(3)}Fe_{3.122(3)}N$ the lattice parameter is a = 3.8818(1) Å. Using various experimental and theoretical methods, it was concluded that tin exclusively substitutes iron atoms on Wyckoff position 1a while position 1b is fully occupied by nitrogen as evident from prompt-gamma-ray activation analysis (PGAA). Susceptibilities and saturation magnetizations of $Sn_xFe_{4-x}N$ compounds reveal a linear weakening of ferromagnetic interactions with increasing tin concentration.

■ AUTHOR INFORMATION

Corresponding Author

*E-mail: drons@HAL9000.ac.rwth-aachen.de. Fax: (+49) 241-80-92642.

Author Contributions

The manuscript was written through contributions of all authors. All authors have given approval to the final version of the manuscript.

Notes

The authors declare no competing financial interest.

■ ACKNOWLEDGMENTS

The authors thank Dr. P. Müller for the X-ray measurements; Ch. Houben, Dr. J. van Leusen, and T. Storp for the SQUID data; H. Bolvardi for the TG-DSC analysis; and Dr. P. Kudejova for the PGAA. The computing center of RWTH Aachen University is gratefully acknowledged for providing us with their supercomputing facilities. The financial support by Deutsche Forschungsgemeinschaft and RWTH Graduiertenförderung (scholarship to T.S.) is gratefully acknowledged.

■ REFERENCES

(1) Chen, S. K.; Jin, S.; Tiefel, T. H.; Hsieh, Y. F.; Gyorgy, E. M.; Johnson, D. W. *J. Appl. Phys.* **1991**, *70*, 6247−6249.

(2) Guillard, C.; Creveaux, H. *C. R. Hebd. Seances Acad. Sci.* **1946**, *222*, 1170−1172.

(3) Andriamandroso, D.; Matar, S.; Demazeau, G.; Fournès, L. *IEEE Trans. Magn.* **1993**, *29*, 2−6.

(4) Siberchicot, B.; Matar, S. F.; Fournès, L.; Demazeau, G.; Hagenmüller, P. *J. Solid State Chem.* **1990**, *84*, 10−15.

(5) Matar, S.; Fournès, L.; Chérubin-Jeannette, S.; Demazeau, G. *Eur. J. Solid State Inorg. Chem.* **1993**, *30*, 871−881.

(6) Burghaus, J.; Wessel, M.; Houben, A.; Dronskowski, R. *Inorg. Chem.* **2010**, *49*, 10148−10155.

(7) Stadelmaier, H. H.; Fraker, A. C. *Z. Metallkde.* **1962**, *53*, 48−51.

(8) Zhao, Z. J.; Xue, D. S.; Li, F. S. *J. Magn. Magn. Mater.* **2001**, *232*, 155−160.

(9) Pauling, L. *J. Am. Chem. Soc.* **1947**, *69*, 542−553.

(10) Cordero, B.; Gómez, V.; Platero-Prats, A. E.; Revés, M.; Echeverría, J.; Cremades, E.; Barragán, F.; Alvarez, S. *Dalton Trans.* **2008**, 2832−2838.

(11) Zhao, Z.; Xue, D. S.; Chen, Z.; Li, F. *Phys. Status Solidi A* **1999**, *174*, 249−253.

(12) Andriamandroso, D.; Fefilatiev, L.; Demazeau, G.; Fournès, L.; Pouchard, M. *Mater. Res. Bull.* **1984**, *19*, 1187−1194.

(13) Kuhnen, C. A.; dos Santos, A. V. *Solid State Commun.* **1993**, *85*, 273−279.

(14) Kuhnen, C. A.; dos Santos, A. V. *J. Alloys Compd.* **2000**, *297*, 68−72.

(15) dos Santos, A. V.; Krause, J. C. *J. Magn. Magn. Mater.* **2004**, *283*, 297−304.

(16) Houben, A.; Šepelák, V.; Becker, K.-D.; Dronskowski, R. *Chem. Mater.* **2009**, *21*, 784−788.

(17) Houben, A.; Burghaus, J.; Dronskowski, R. *Chem. Mater.* **2009**, *21*, 4332−4338.

(18) Burghaus, J.; Kleemann, J.; Dronskowski, R. *Z. Anorg. Allg. Chem.* **2011**, *637*, 935−939.

(19) Music, D.; Burghaus, J.; Takahashi, T.; Dronskowski, R.; Schneider, J. M. *Eur. Phys. J. B* **2010**, *77*, 401−406.

(20) Rodriguez-Carvajal, J. *FULLPROF Version 5.60*; 2015, ILL.

(21) Molnár, G. L. *Handbook of Prompt Gamma Activation Analysis with Neutron Beams*; Kluwer Academic Press: Dordrecht, Boston, 2004.

(22) Liu, S. *Phys. Rev. B* **1977**, *15*, 4281−4287.

(23) Kresse, G.; Furthmüller, J. *Comput. Mater. Sci.* **1996**, *6*, 15−50.

(24) Kresse, G.; Hafner, J. *Phys. Rev. B: Condens. Matter Mater. Phys.* **1993**, *47*, 558−561.

(25) Blöchl, P. E. *Phys. Rev. B: Condens. Matter Mater. Phys.* **1994**, *50*, 17953−17979.

(26) Kresse, G.; Joubert, J. *Phys. Rev. B: Condens. Matter Mater. Phys.* **1999**, *59*, 1758−1775.

(27) Perdew, J. P.; Burke, K.; Ernzerhof, M. *Phys. Rev. Lett.* **1996**, *77*, 3865−3868.

(28) Monkhorst, H. J.; Pack, J. D. *Phys. Rev. B* **1976**, *13*, 5188−5192.

(29) Wriedt, H. A.; Gokcen, N. A.; Nafziger, R. H. *Bulletin of Alloy Phase Diagrams: The Fe-N (Iron-Nitrogen) System*; 1987; Vol. 8.

(30) Xu, Y.; Elbicki, J. M.; Wallace, W. E.; Simizu, S.; Sankar, S. G. *IEEE Trans. Magn.* **1992**, *28*, 2569−2571.
(31) Wollan, E. O.; Koehler, W. C. *Phys. Rev.* **1955**, *100*, 545−563.